Assessing the potential of non-pyrophoric Zn(DMP) 2 for the fast deposition of ZnO functional coatings by spatial atomic layer deposition

Liam Johnston, Jorit Obenlüneschloß, Muhammad Farooq Khan Niazi, Matthieu Weber, Clément Lausecker, Laetitia Rapenne, Hervé Roussel, Camilo Sanchez-Velazquez, Daniel Bellet, Anjana Devi, et al.

RSC Applied Interfaces

ROYAL SOCIETY OF CHEMISTRY

PAPER

View Article Online
View Journal | View Issue

Cite this: *RSC Appl. Interfaces*, 2024, **1**, 1371

Assessing the potential of non-pyrophoric $Zn(DMP)_2$ for the fast deposition of ZnO functional coatings by spatial atomic layer deposition†

Liam Johnston, [a] Jorit Obenlüneschloß, [b] Muhammad Farooq Khan Niazi, [a] Matthieu Weber,[a] Clément Lausecker,[a] Laetitia Rapenne,[a] Hervé Roussel,[a] Camilo Sanchez-Velazquez,[a] Daniel Bellet, [a] Anjana Devi [bc] and David Muñoz-Rojas *[a]

Received 7th May 2024,
Accepted 23rd July 2024

DOI: 10.1039/d4lf00160e

rsc.li/RSCApplInter

Spatial atomic layer deposition (SALD) is a promising thin film deposition technique that enables fast, large-scale deposition and nanoscale thickness control by utilizing spatially separated precursor vapors and a substrate-specimen relative motion, while being feasible in atmospheric pressure conditions. This study explores the use of a non-pyrophoric precursor, $Zn(DMP)_2$, in open-air SALD to produce ZnO, and compares the SALD processing speed, and thin film properties, as well as the environmental impact of using this precursor *versus* the more conventional diethylzinc (DEZ), whose pyrophoricity discourages open-air processing. For this purpose, a life cycle analysis (LCA) study was carried out. Our investigation shows that $Zn(DMP)_2$ open-air SALD can yield ZnO films faster than conventional ALD using DEZ, producing high purity ZnO films with a growth per cycle of 0.7 Å at 180 °C, which corresponds to 184 Å min^{-1} maximal growth rate. Emphasizing practical applications, the conformality of the ZnO coating produced around silver nanowire (AgNW) networks by $Zn(DMP)_2$ open-air SALD and the functionality of these protective coatings has also been demonstrated. The resulting transparent conductive nanocomposites had a substantially improved durability on par with their DEZ-synthesized counterparts.

Introduction

Atomic layer deposition (ALD) is a deposition technique enabling the coating of high quality thin films on challenging substrates with excellent conformality and nanoscale thickness control.[1] ALD can be applied to prepare a large variety of materials, such as metal oxides,[2] metals,[3] nitrides,[4] and sulphides.[5] Among these materials, zinc oxide (ZnO) is the one that has been one of the most deposited by ALD owing to its broad range of applications, such as in photovoltaics,[6] piezoelectric sensors,[7] and transparent electronics.[8]

Currently, the overwhelming majority of ZnO ALD processes use diethylzinc (DEZ) as the Zn precursor,[9] whose popularity stems from its high reactivity and volatility, allowing for very short pulse times in temporal ALD to achieve surface saturation and thus higher growth rates (which can be expressed in Å min^{-1}) than many other ALD processes. However, DEZ is also known for being highly pyrophoric, leading to higher costs associated with safety and transport, particularly when using open-air setups (*i.e.* setups characterized by the absence of a physical barrier between the reaction region and the outside air). Therefore, alternative non-pyrophoric precursors are needed. In this sense, the current state of the art in Zn precursors for ALD is represented in Table 1, where one non-pyrophoric precursor stands out for its high growth per cycle (GPC) despite low deposition temperatures: $Zn(DMP)_2$ or bis-3-(*N*,*N*-dimethylamino)propyl zinc as suggested by Mai *et al.* for plasma-enhanced ALD (PEALD).[10]

$Zn(DMP)_2$ is non-pyrophoric and solid at room temperature (demonstrated in Fig. S13†) while having a low melting point of 45 °C, making it safer and easier to work with than DEZ, in particular when using an open-air setup. It could be used in a $Zn(DMP)_2$ + H_2O thermal ALD process to yield a GPC of 1.1 Å,[14] which is still less than the GPC of 1.8–2.0 Å that is typically obtained with DEZ (though this value varies strongly in the literature).[9] While $Zn(DMP)_2$ has shown a great potential as a replacement to DEZ in temporal ALD processes (*i.e.* ALD involving sequential precursor pulses and purges that span the entire substrate),[14,17] its suitability for

[a] *Grenoble INP, CNRS, LMGP – Grenoble, Univ. Grenoble Alpes, France. E-mail: david.munoz-rojas@grenoble-inp.fr*
[b] *Inorganic Materials Chemistry, Ruhr Univ. Bochum, 44801, Bochum, Germany*
[c] *Leibniz Institute for Solid State and Materials Research, 01069, Dresden, Germany*

† Electronic supplementary information (ESI) available. See DOI: https://doi.org/10.1039/d4lf00160e

Table 1 Current state-of-the-art zinc precursors and proposed ALD parameters found in literature

Zn precursor	Pyrophoricity	Co-reactant	Precursor delivery T (°C)	Substrate T (°C)	GPC (Å)	Ref.
$Zn(C_2H_5)_2$ (DEZ)	**Yes**	**H_2O**	**Ambient**	**110–170**	**1.8–2**	9, 11, 12
		O_2 plasma	—	**75–150**	**1.9–2.2**	13
$Zn(DMP)_2$	**No**	**H_2O**	**35**	**60–140**	**0.49–1.1**	14
		O_2 plasma	—	**60–140**	**0.42–0.69**	10
$EtZn(damp)_2$	No	H_2O_2	135	200	1.25	15
$Zn(eeki)_2$	No	H_2O	100	175–300	1.3	16
$Zn(CH_3)_2$	Yes	H_2O	−25	80–150	1.8	8
$Zn(OOCCH_3)_2$	No	H_2O	230–250	280–350	1.8	8

fast-deposition over large areas, such as the obtained with spatial ALD (SALD), is yet to be evaluated. This is the prevailing aim of the work.

SALD is a recent approach that can offer the same advantages as ALD, but with growth rates typically in the 60–600 Å min^{-1} range which are comparable to CVD rates.[18] At the same time, processing is even feasible in the open-air[19] allowing for easier up-scaling and no extra costs associated to vacuum techniques. Various approaches can be considered to perform SALD. In this work, the close-proximity approach is used,[20] by continuously injecting the precursors at different points on the substrate surface, and moving the substrate to cyclically expose it to the desired precursor pulse steps, which drastically reduces the needed pulse time to saturate the surface. In this approach, the precursors are separated by a N_2 inert gas barrier preventing the precursors from meeting in the gas phase and preventing the outside air from reacting with the metal precursor.

In this study, the open-air SALD using a non-pyrophoric precursor such as $Zn(DMP)_2$ was investigated to test whether (i) good quality ZnO thin films can indeed be produced, and (ii) to compare the obtained films to films produced using conventional ALD using DEZ in terms of growth rate, structural properties, and chemical properties. The conformality of the deposition technique around silver nanowire (AgNW) networks was also investigated as well as the functionality of the fabricated ZnO/AgNW nanocomposite networks, which is tested by characterizing the stability of these nanocomposites under electrical stress.

Experimental details

Precursor synthesis

$Zn(DMP)_2$ is synthesized through a salt metathesis reaction of zinc chloride ($ZnCl_2$) with the Grignard reagent [(DMP)MgCl] in Et_2O or tetrahydrofuran (THF), as first described by Hofstee *et al.*[21] and later optimized by Mai *et al.*[10,22] The high sensitivity to moisture of this reaction required the use of Schlenk techniques under a dry argon atmosphere (Air Liquide 99.995%). The Grignard solution was prepared from a reaction of (DMP)Cl with activated magnesium metal filings and added to the ZnCl.[22] The salt by-products of this reaction (Fig. 1) could be precipitated out of solution by evaporating the polar solvent under reduced pressure and replacing it with hexane. This enables the filtration and extraction of the soluble crude $Zn(DMP)_2$ product which was purified by sublimation at 80 °C under mild vacuum (roughly 10^{-2} mbar) after removal of the hexane solvent under reduced pressure. This synthesis approach can produce a yield of 62% as reported by Mai *et al.*[10]

SALD setup

For the development of SALD processes, a home-made setup was used in this work similar to other previous works.[13,15,23] Our close-proximity SALD setup is schematically represented in Fig. 2. The substrate oscillates back and forth along a horizontal axis with a speed v_S, while the manifold above is aligned at a fixed distance forming a constant gap around 150 μm with the substrate. The manifold outflows form a periodic pattern of regions at the substrate surface corresponding to the prototypical ALD cycle of co-reactant pulse/N_2 purge/metal precursor pulse/N_2 purge.

The manifold used in this study contained two metal precursor outflows, such that one pass corresponds to 2 successive ALD cycles, and therefore one oscillation yields 4 ALD cycles. Since the ALD cycle must start with the co-reactant independently of the direction of movement, there are 3 total co-reactant outflows. To prevent cross-talking of the precursors and ensure ALD conditions, these 2 precursor lines and 3 co-reactant lines are separated by a total of 6 N_2 inert gas barriers, while an additional 12 exhausts are placed to evacuate the excess chemical species and ALD by-products.

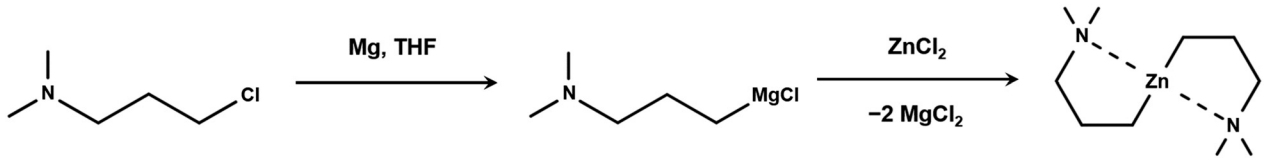

Fig. 1 Scheme of the synthesis of the Grignard reagent (DMP)MgCl from (DMP)Cl and Grignard reaction producing $Zn(DMP)_2$.

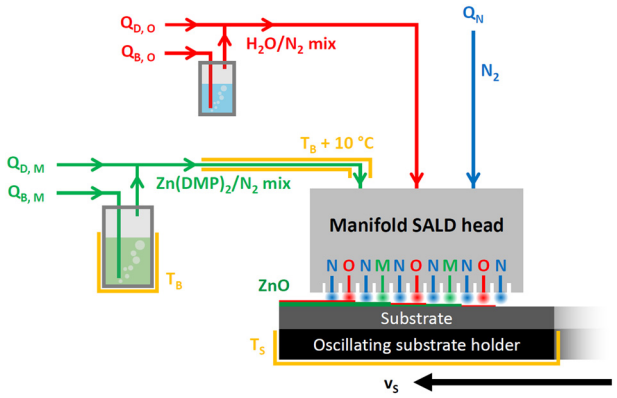

Fig. 2 Schematic of the close-proximity SALD setup at LMGP. At the substrate surface, three types of gas regions exist corresponding to the metal precursor in green (M), the oxygen source in red (O), and the inert nitrogen gas barrier (N). Heaters are schematically colored in gold.

All manifold outlet lines have a channel thickness of 0.5 mm and a width of 30 mm.

N_2 is used both as the carrier gas for the reactive species and as the barrier flow preventing precursor cross-talk. A flow rate Q_N was split between the 6 inert gas barriers by the manifold, while the precursors were volatilized in N_2 gas using bubblers for the metallic precursor $Zn(DMP)_2$ (subscript M, for metal source), the co-reactant H_2O (subscript O, for oxygen source), each with separated flow rate units to the bubbler $Q_{B,M}$ and $Q_{B,O}$. These precursor vapors were further diluted with N_2 mass flows $Q_{D,M}$ and $Q_{D,O}$. Three heaters, corresponding to the substrate (T_S), the bubbler (T_B), and the line, are used to maintain a constant temperature of these components. The line is kept around 10 °C hotter than the bubbler to prevent recondensation of the volatilized species. The substrate holder is heated to a temperature T_S. Owing to the lower volatility of $Zn(DMP)_2$ *versus* DEZ,[10] the bubbler had to be heated to satisfyingly produce the precursor vapors needed. The complete set of parameters along with substrate oscillation speed v_S and gas flow rates are given in Table S1.†

Sample characterization

The evolution of the film thickness, density, crystallinity, and surface morphology *versus* the substrate temperature (T_S) was probed using ellipsometry, X-ray reflectivity (XRR), grazing-incidence X-ray diffraction (GIXRD), and scanning electron microscopy (SEM), while the stoichiometry was probed using X-ray photoelectron spectroscopy (XPS). All samples were deposited on soda-lime glass at atmospheric pressure. Thickness values were obtained through ellipsometry, using a compact Film Sense FS-1™ *ex situ* ellipsometer and the data was fitted using a Cauchy model. SEM images were taken/recorded using a ZEISS GeminiSEM 300 equipped with a Bruker Quantax® EDXS detector. Density measurements were obtained by measuring the XRR critical angle to a specific stoichiometric ZnO density using a methodology described in the ESI† linked to this work. GIXRD was performed at a grazing angle of 0.4°. Both XRR and GIXRD were performed using a Rigaku SmartLab® diffractometer. The chemical purity of the films was probed *via* X-ray photoelectron spectroscopy (XPS) using a ThermoFisher Scientific K-Alpha™ spectrometer equipped with a monochromatic Al K_α X-ray source at 1486.6 eV. An Ar^+ surface sputter cleaning process was used for 30 s to remove the mostly carbon-based surface contaminants and allowing probing the bulk stoichiometry of the sample.

SALD on AgNWs and nanocomposite characterization

A $Zn(DMP)_2/H_2O$ open-air SALD process at 150 °C was used to produce ZnO coatings with varying thicknesses around silver nanowire (AgNW) networks. The nanowires were obtained commercially from PROTAVIC® as a suspension in isopropanol and then sprayed onto a heated Corning® glass substrate using a home-made setup until a sheet resistance of roughly 10 Ω sq^{-1} was reached, as described by Bardet *et al.*[24] The morphology of the nanocomposites was probed using SEM as described previously, as well as using transmission electron microscopy (TEM) with a JEOL JEM-2010 LaB_6 device. By demonstrating the effectiveness of ZnO coatings grown using $Zn(DMP)_2$ as Ag diffusion barriers in AgNW networks, the conformality and applicability of SALD for these nanocomposites using this precursor can then be clearly proven.

To test the electrical stability of the nanocomposites, a voltage ramp of 0.1 V min^{-1} was applied between two electrodes (prepared through the application of silver paste) separated by 2 cm of ZnO-coated AgNW networks on a soda-lime glass substrate for different ZnO coating thicknesses. The electrical setup used here was similar to that of Khan *et al.*[25] except the samples and electrodes here were half the width (perpendicular to the current flow). Since the electrodes are separated by a similar distance as previous experiments and the voltage conditions are identical, the local electric field and thus the local Joule heating effect is also similar. The networks were thus brought to a breaking point situated at a certain "failure" voltage along the chosen voltage ramp as per previous experiments on bare AgNW networks[26] and ZnO-coated AgNW networks using DEZ as the Zn source.[25]

Results and discussion

ZnO thin films

Process development. Open-air SALD experiments were performed using $Zn(DMP)_2$ between temperatures of 80 and 260 °C. These experimental results are displayed in Fig. 3 and compared between each other and against a selection of literature in order to assess the performance of $Zn(DMP)_2$ open-air SALD against other deposition techniques such as conventional ALD, plasma-enhanced ALD (PEALD), and also against ALD and SALD using DEZ as the Zn precursor.

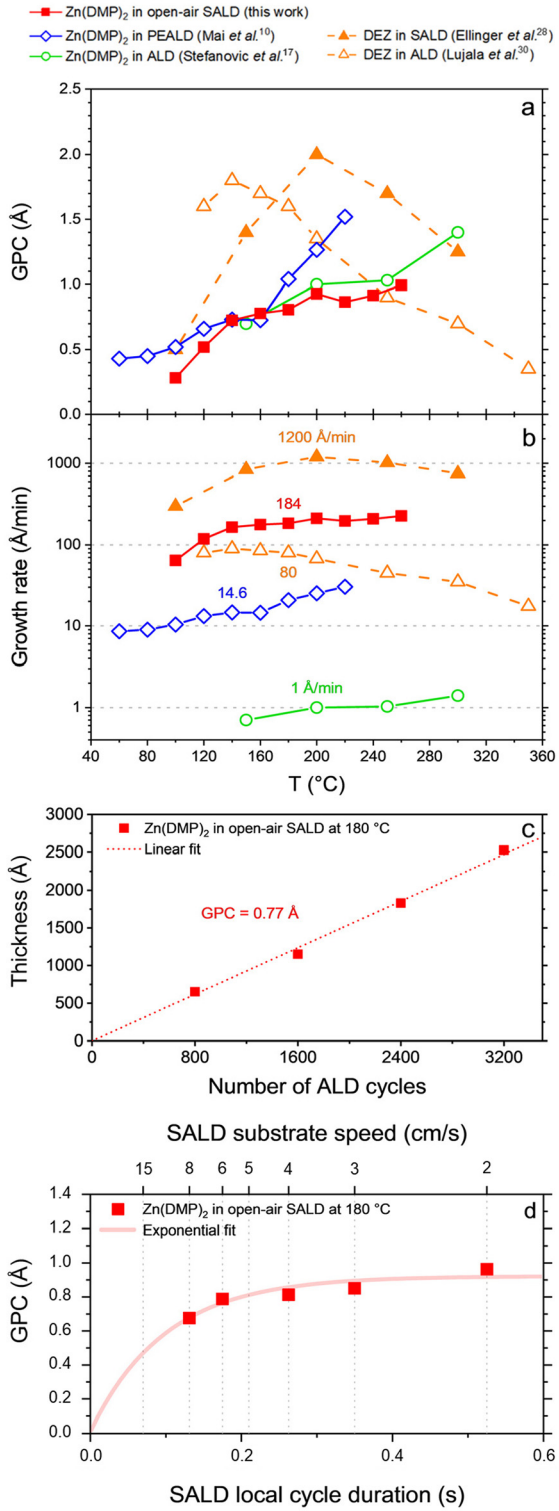

Fig. 3 Comparison of growth per cycle (GPC) (a) values and growth rates (b) for various ALD (open symbols) and SALD (closed symbols) processes using $Zn(DMP)_2$ (solid lines) or DEZ (dashed lines) at different deposition temperatures in literature.[10,17,27,28] The thickness of samples deposited using $Zn(DMP)_2$ open-air SALD is also tracked against the number of ALD cycles deposited (c) to extract precise GPC values and to prove high thickness control of the deposition approach. The evolution of the GPC with the platen speed (d), revealed a saturation trend at slower speeds which confirms the ALD behaviour of our process (the *x* axis was inverted to use a metric proportional to the $Zn(DMP)_2$ pulse time).

$Zn(DMP)_2$ open-air SALD has been used to produce ZnO thin films with H_2O as co-reactant. At first, the GPC was found to increase with the temperature until 140 °C, after which a relative plateau was reached, which seems to correspond to the beginning of the ALD window for this process. In the 140–180 °C range the GPC value is steady between 0.7 and 0.8 Å, with a more precise investigation of the GPC shown in Fig. 3c yielding a GPC of 0.77 Å at 180 °C. Temperatures above 260 °C could not be probed using the present open-air SALD setup, although a certain amount of precursor decomposition above 180 °C could be expected, as observed in the PEALD data from Mai *et al.*[10] Though this phenomenon is not observed at 180 °C in our setup using H_2O as a co-reactant, we may still expect a similar temperature dependent GPC increase for longer precursor exposures, as possibly indicated by the mild increase still visible between 180 and 260 °C.

The $Zn(DMP)_2$ exposure time necessary to reach surface saturation was found to decrease as the temperature increased from 140 °C to 180 °C (*cf.* ESI,† Fig. S5) which is indicative of a chemisorption-based adsorption process within this temperature window.[27] As such, this could explain why a small GPC increase is visible in this window as the exposure time was kept constant while the growth kinetics were sped up, while lower temperatures would in fact need longer exposure times to reach the same degree of saturation.

When increasing from 180 °C to 260 °C, however, the saturation time was found to increase, indicating instead a physisorption process, which does not lead to the self-limiting growth necessary for ALD. Therefore, while an ALD window can be traced from 140 °C to at least 180 °C, this window does not extend up to 260 °C using the present setup.

When the growth rate of $Zn(DMP)_2$ is compared to that of DEZ, processes using the former precursor tend to yield a lower throughput (*cf.* Fig. 3b) due to the longer pulse times required to saturate the same surface (due to lower precursor volatility and reactivity) and due to the lower GPC value of $Zn(DMP)_2$ overall with respect to DEZ. Despite this limitation, open-air SALD using $Zn(DMP)_2$ could still yield a growth rate roughly twice as fast as ALD using DEZ at the same deposition temperature of 180 °C. As discussed in the introduction, this is because switching from ALD to SALD significantly increases the deposition throughput notably by avoiding the long purge times needed in the ALD cycle. Elsewhere, $Zn(DMP)_2$ SALD is understandably slower than DEZ SALD though it reached growth rates between 1 and 2 orders of magnitude higher than temporal ALD approaches.

It should be noted that the growth rate in SALD is calculated by using an optimal SALD cycle time defined by the spatial period of an ALD cycle on the SALD manifold divided by the substrate speed. This approach gives a real cycle time value but (for the sake of comparison between SALD and ALD processes) neglects that in some architectures, such as the one described here and in the DEZ SALD instance

from Ellinger *et al.*,[28] parts of the substrate may be outside the deposition region leading to a lower effective growth rate. Data on conventional ALD with $Zn(DMP)_2$ is reported from Stefanovic *et al.*[12] who used a purge time of 20 s in between three short precursor pulses (double $Zn(DMP)_2$ pulse + H_2O pulse) leading to around 60 s of cycle time.

Characterization of the thin film physico-chemical properties. The crystallinity and texture of some of the ZnO thin films prepared by open-air SALD using $Zn(DMP)_2$ were investigated in the 140–260 °C temperature range by GIXRD, and the surface morphology was studied using SEM for two samples (see Fig. 4).

Samples prepared at a substrate temperature of 140–220 °C were found to exhibit almost no ZnO (002) peak as expected at a diffraction angle of 2θ = 34.4° (ICDD reference no. 00-036-1451). This corresponds to a suppression of the crystal growth along the *c*-axis of the hexagonal ZnO lattice and/or a low probability for crystallites to be oriented with a vertical *c*-axis (*i.e.* perpendicular to the substrate surface). Preferential growth along the *c*-axis was only achieved after heating the substrate to 260 °C, at which point a highly textured thin film was obtained along the ⟨001⟩ direction, whose properties are particularly useful for piezoelectric applications.[29] The suppression of *c*-axis growth at lower ALD temperatures is in fact often observed in ALD experiments using DEZ as a precursor, where textured growth along the ⟨001⟩ direction typically only begins from 200 °C approximately.[9,17,30,31]

The ZnO surface morphology evolved to reflect this change in texture (*cf.* Fig. 4d). This temperature was however much higher than the precursor decomposition onset temperature of 180 °C suggested by Mai *et al.*,[10] which may also explain a parasitic deposition of non-volatile precursor fragment aggregates in our experiments at 260 °C as reported in Fig. S6,† though such a decomposition could not be observed in our experiments at 180 °C.

The density of films deposited in the 140–260 °C range was consistently around 5.1 g cm^{-3} as shown in Fig. S3 and S4a.† This value is lower than those typically obtained through ALD[32] and open-air SALD[33] using DEZ which is reported in the range of 5.41 to 5.61 g cm^{-3}. This discrepancy may be explained from the potentially lower grain size in the films derived from $Zn(DMP)_2$, leading to a higher preponderance of grain boundaries in the mass of the thin film due to lower GPC values as evidenced in experiments using DEZ.[33] This may in turn lead to poorer conductive properties for the $Zn(DMP)_2$-derived ZnO.

Chemical analysis of a sample deposited using a $Zn(DMP)_2/H_2O$ process at 150 °C was performed using XPS and the peaks obtained could be fitted using mixed Gaussian/Lorentzian contributions (Fig. 5) which were associated to atomic orbitals in different chemical environments, except for the N 1s orbital, which was below the detection limit around 0.3% (atomic). The area of these contributions could be linked to a direct atomic percentage of each atom, differentiated in terms of chemical environment when applicable, as given in Table S2.†

This revealed a relatively low carbon contamination in the film (less than 2.5% at) in C–C and C–H bonds for the most part while a slightly lesser C═O contribution was also found. This C contamination may be due to leftover organic surface contaminants after the sputter cleaning or potentially from

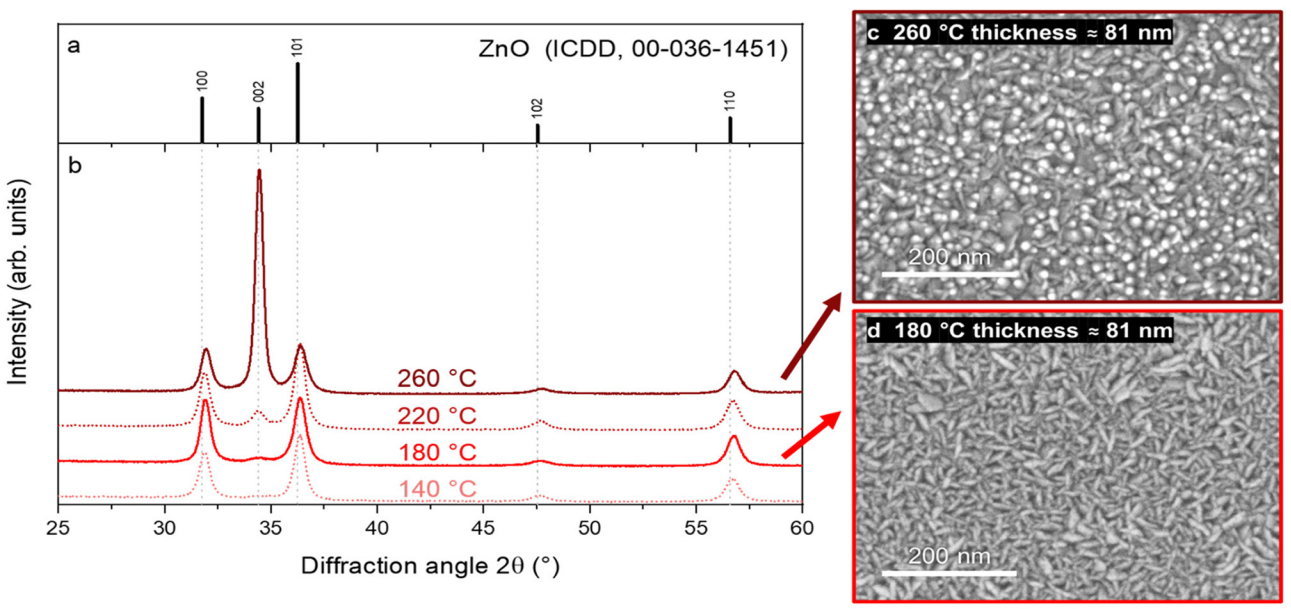

Fig. 4 GIXRD patterns of ZnO thin films deposited at various temperatures (b) compared with the theoretical diffraction pattern for ZnO in the wurtzite structure as per the ICDD database (a). The thin films showed mainly *a*-axis growth for all temperatures except 260 °C where *c*-axis growth was achieved. This texture change is visible in the surface morphology as studied using SEM on samples grown at 260 °C (c) and 180 °C (d).

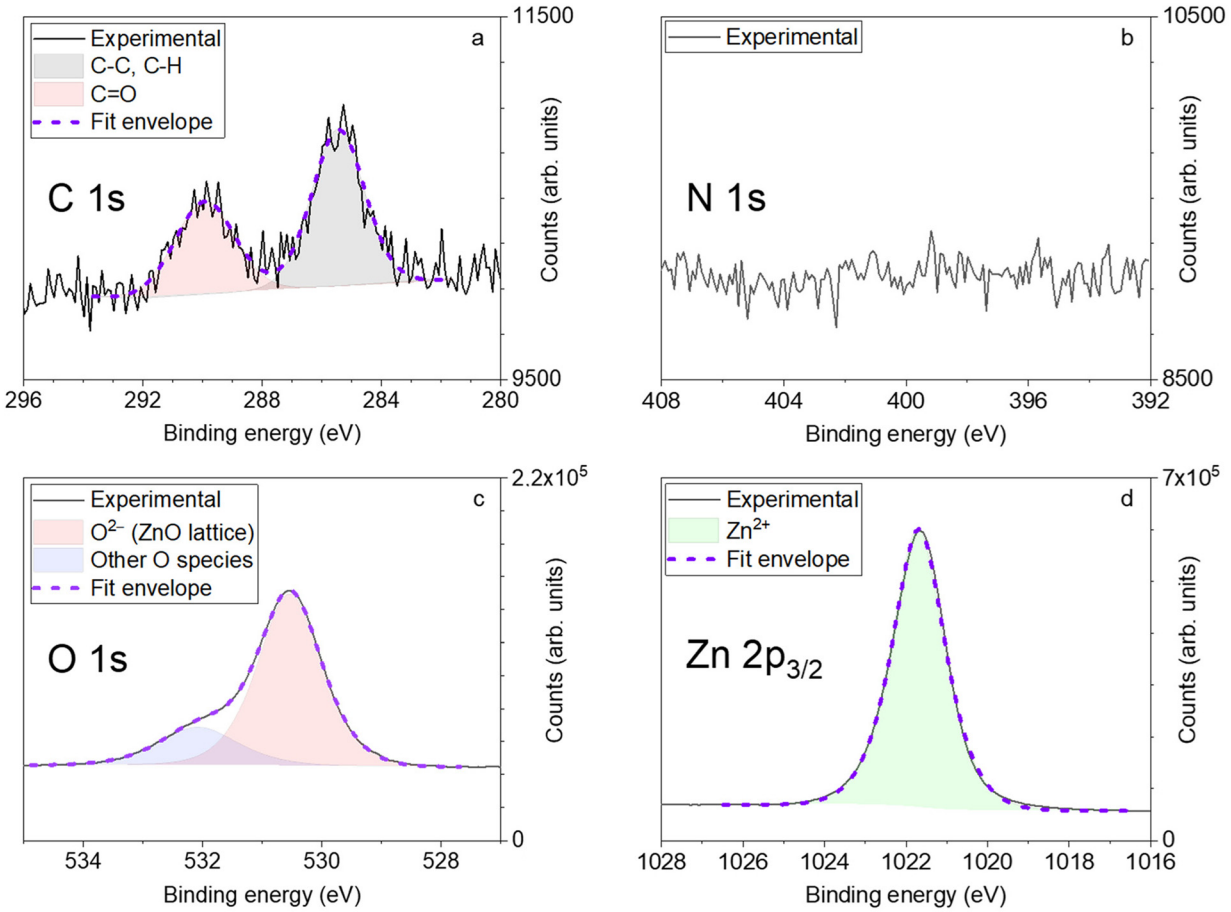

Fig. 5 XPS spectra of ZnO sample using $Zn(DMP)_2$ deposited at 150 °C: the carbon 1s orbital (a), the nitrogen 1s orbital (b), the O 1s orbital (c), and the 3/2 peak of the Zn 2p orbital (d) are shown.

precursor fragments, although no precursor-derived N could be detected.

The O 1s orbital could be deconvoluted into two main contributions, one around 530.5 eV from the oxygen in the wurtzite crystal lattice of ZnO and another around 532.1 eV, which may be linked to OH and O^- species from absorbed hydroxides and O_2 in the film or metal carbonates, but could also be the consequence of atmospheric processing, resulting in adsorbed oxygen on grain boundaries as suggested in previous experiments using open-air SALD.[34] By fitting the Zn $2p_{3/2}$ orbital, we could determine the stoichiometry of ZnO at O/Zn = 1.03 within the wurtzite lattice and O/Zn = 1.31 taking all O contributions into account. A similarly O-rich film was obtained at this temperature by Stefanovic *et al.* through both temporal and spatial ALD approaches which they attributed to absorbed hydroxides and oxygen vacancies.[12]

ZnO/AgNW nanocomposites

In this section, the conformality and quality of the films deposited with $Zn(DMP)_2$ using SALD is put to the test on a non-planar substrate: AgNWs. This type of work has already been reported using DEZ as the Zn source.[25] As such, it is known that the ZnO coating delays the Ag atomic diffusion at the surfaces of AgNW and can significantly improve the stability of the nanowires against thermal stress (which can be produced through annealing)[24] or electrically-induced thermal stress. It was also observed that the thicker the ZnO layer the more stable the AgNW network. Such an observation was explained thanks to a simple physical model assuming the diffusion of Ag atoms through the ZnO coating as a voltage-independent Fickian diffusion coefficient D_{Ag-ZnO} (see eqn (1)).

The same approach has been used in this work to assess the quality of the deposited ZnO thin films, which was deposited using a modified $Zn(DMP)_2$ open-air SALD process at 150 °C described in the ESI† report linked to this paper and which yielded a GPC of 0.40 Å.

It is worth noticing that the temperature used by Khan *et al.*[25] (200 °C) was significantly higher than the one used here (150 °C); this is a clear asset to consider low temperature deposition since it enables to consider sensitive substrates (such as polymeric substrate or organic compounds). These nanocomposites may indeed be incorporated in flexible transparent conductive devices which could be used in new-

generation photovoltaic cells, touch-screen displays, OLEDs, smart-windows, and transparent heaters.[35,36]

Morphology of the ZnO/AgNW nanocomposites

The ZnO-coated AgNW networks were studied using secondary electrons (SE) and backscattered (BS) SEM, and also using transmission electron microscopy (TEM) combined with selective-area electron diffraction (SAED) for 3 different ZnO coatings obtained from 320, 640, and 960 $Zn(DMP)_2/H_2O$ ALD cycles (Fig. 6). At an expected GPC value of 0.40 Å, these coatings would have a thickness of 12.8, 25.6, and 38.4 nm respectively.

The TEM and back-scattered SEM images revealed a ZnO thickness that increased with more ALD cycles at a rate consistent with that observed from thin films. The SAED patterns presented point-wise diffraction peaks corresponding to a monocrystalline phase as well as a series of concentric rings corresponding to a second polycrystalline phase which could be attributed to the signal from the AgNW and the ZnO coating respectively (the detail of image D1 and the relevant analysis are given in Fig. S11† for one sample). The coatings were conformal as evidenced by the consistent coating thicknesses around all nanowires but had a higher roughness for thicker coatings as seen in images C2 and C3 in particular. This may be due to the suppressed growth along the *c*-axis discussed before, which results in the growth of flake-like hexagonal grains that extend horizontally and thus cause higher roughness around substrates with high curvatures (such as nanowires) than on planar substrates.

Using the BS SEM from Fig. 6 (images B1–B3), we could extract a rough estimate of the ZnO coating thickness with

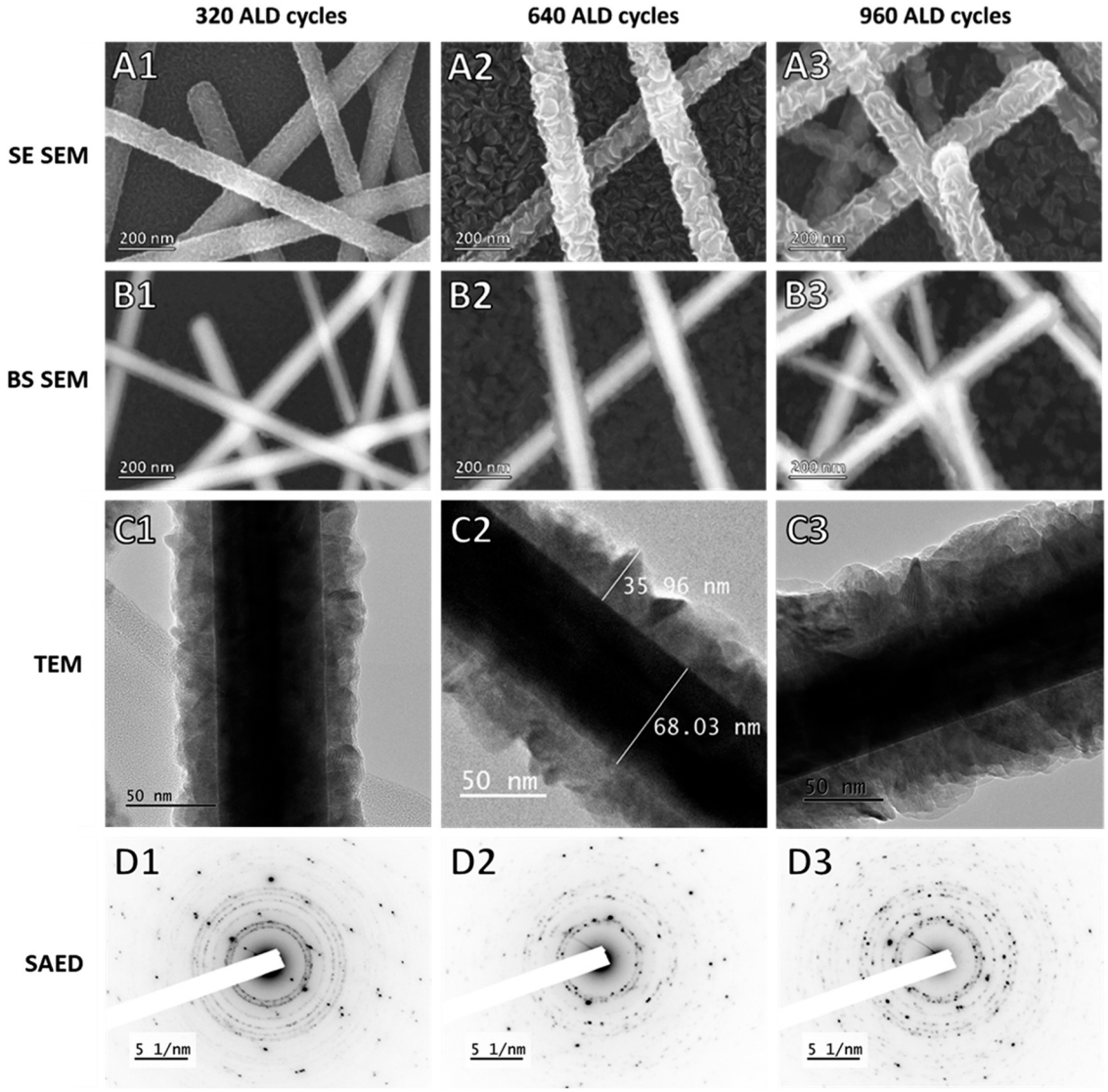

Fig. 6 Evolution of ZnO coating morphology after 320 (–1), 640 (–2), and 960 (–3) ALD cycles at 150 °C using $Zn(DMP)_2$, studied using SE SEM for surface morphology (A1–A3), BS SEM for chemical contrast inside nanowire (B1–B3), TEM of single nanowires to show morphological detail (C1–C3), and SAED to show ZnO coating crystallinity (D1–D3).

respect to the number of cycles (*cf.* Fig. S12†), the slope of which corresponded to the GPC observed for ZnO thin films grown on glass.

Electrical characterization

The AgNW networks exhibit electrical conduction as long as charge carriers are able to navigate the sample through the percolation mechanism. Morphological instability of AgNWs is observed when AgNW networks are subjected to thermal or electrical stress.[37] The driving process leading to electrical failure of the percolating network is the thermally-induced diffusion of Ag atoms at the nanowire surface resulting in the spheroidization of the metal oxide-coated nanowires.

This morphology change occurs in an effort to reduce the Ag surface area as described by the Plateau–Rayleigh instability.[26] Coating this surface with a material such as ZnO introduces a diffusion barrier delaying this morphology change. As such, the diffusion coefficient of Ag through ZnO is an important parameter for the stability enhancement of these networks. This also implies that the protective metal oxide coating must be conformal to avoid higher Ag diffusion through less thickly coated parts. Here, "failure" of the nanocomposites refers here to the point after which the measured sheet resistance dramatically and irreversibly increases exclusively as a consequence of the loss of the percolation phenomenon across the sample.

The dependence between the AgNW network electrical resistance *versus* voltage during a voltage ramp of $\dot{V}$ = 0.1 V min^{-1} is plotted in Fig. S12.† An increase of the resistance with the voltage is observed due to the Joule effect increasing the temperature in the AgNWs. For larger voltages, electrical failure of the nanocomposite networks is observed for a given voltage, named failure voltage. Fig. 7 exhibits the failure voltage *versus* the ZnO coating thickness (L_{ZnO}). As with experiments using ZnO derived from DEZ,[25] thicker Zn(DMP)$_2$-derived ZnO coatings around the AgNW did indeed delay the spheroidization of the nanowires and thus delayed the electrical failure of the sample, from 9 V in the non-coated case to 17.2 V for a ZnO coating thickness around 35 nm.

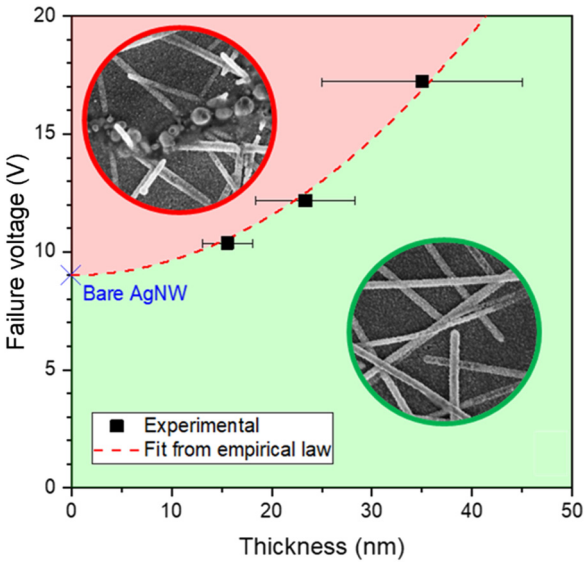

Fig. 7 Evolution of failure voltage *vs.* ZnO coating thickness around AgNWs, with the green region corresponds to a percolating network and the red region to non-percolating networks (*i.e.* after failure), and fitting our data with eqn (1).

Other ramp values will change this trend as the diffusion process is time-dependent. According to Khan *et al.*,[25] a parabolic dependence law (eqn (1)) can be used to fit the experimental points by using the value of bare AgNW networks ($V^{fail}_{bare\ AgNW}$ = 9 V) in their case, which given the similarity of the experimental conditions can also be considered to be the case here. The dependence of the failure voltage $V^{fail}_{coated\ AgNW}$ of the nanowire network coated with a ZnO coating of thickness L_{ZnO} can be expressed as

$$V^{fail}_{coated\ AgNW}(L_{ZnO}) = V^{fail}_{bare\ AgNW} + \frac{\dot{V}\cdot {L_{ZnO}}^2}{2D_{Ag-ZnO}} \quad (1)$$

where in our case the diffusion coefficient D_{Ag-ZnO} could be fitted to 1.30 × 10^{-15} cm^2 s^{-1} for nanocomposites that used Zn(DMP)$_2$ as a ZnO precursor. The obtained diffusion coefficient value is very close to the one deduced by Khan *et al.* (0.99 × 10^{-16} cm^2 s^{-1}).[25] The small difference can be attributed to the higher roughness of the Zn(DMP)$_2$-derived ZnO coatings at higher thicknesses or to the lower density of the Zn(DMP)$_2$ films resulting in an easier diffusion of the Ag atoms through the metal oxide coating. The high roughness of the films as recorded in the horizontal error bars in Fig. 7 reflects the roughness visible in the TEM images in Fig. 6 which, in turn, stems from the anisotropic crystalline growth of the ZnO grains on the Ag surface.

This nonetheless shows the failure voltage was nearly doubled by coating the AgNW network with a 35 nm coating of ZnO made using Zn(DMP)$_2$ as a non-pyrophoric precursor in atmospheric pressure SALD.

Comparative life cycle analysis

The use of life cycle assessment (LCA) in evaluating a chemical precursor involves a comprehensive analysis of its environmental impact throughout its entire life cycle, from raw material extraction and synthesis to its application and eventual disposal, providing valuable insights for sustainable and eco-friendly material synthesis processes. Herein, a comparative LCA study has been performed in order to compare the environmental impact of Zn(DMP)$_2$ *versus* DEZ. As described in more details in previous publications,[38,39] the approach used a cradle-to-gate system to assay the environmental impact of the synthesis of a given precursor and the deposition of a given thin film material. This impact is split into 16 categories such as: ozone depletion; climate change; acidification, which though they produce diverse environmental consequences, are directly compared by giving

each category a certain weight as per the "EF 3.0 Method (adapted)" approach recommended by the European Union.[38]

The LCA of the synthesis step tracked the impact of producing a kilogram of DEZ *versus* a kilogram of $Zn(DMP)_2$. The synthesis approach for DEZ is taken as per the standard Zn–Cu couple approach, whereas the synthesis approach for $Zn(DMP)_2$ was based on salt metathesis reaction described in the experimental section.[40] A second LCA was performed by studying the impact of the open-air SALD process using either precursor to produce sample with identical thicknesses. The comparative LCA results are presented in Fig. 8 and the detailed parameters used for the study are given Fig. S8 through Fig. S10.†

Despite the LCA result showing a similar order of magnitude between the total single scores for the synthesis of DEZ and $Zn(DMP)_2$, the crucial takeaway should be that both routes have very different footprints. In the case of DEZ, the synthesis single score is higher in the "resource use, minerals, and minerals" category than all other contributions combined. This is due to the use copper in the synthesis to activate the zinc and increase the yields,[41] which is currently classified as a "near critical" material for the coming 2025–2050 period by the U.S. Department of Energy due to the heavy exploitation of current copper resources worldwide and its crucial role in electrification.[42]

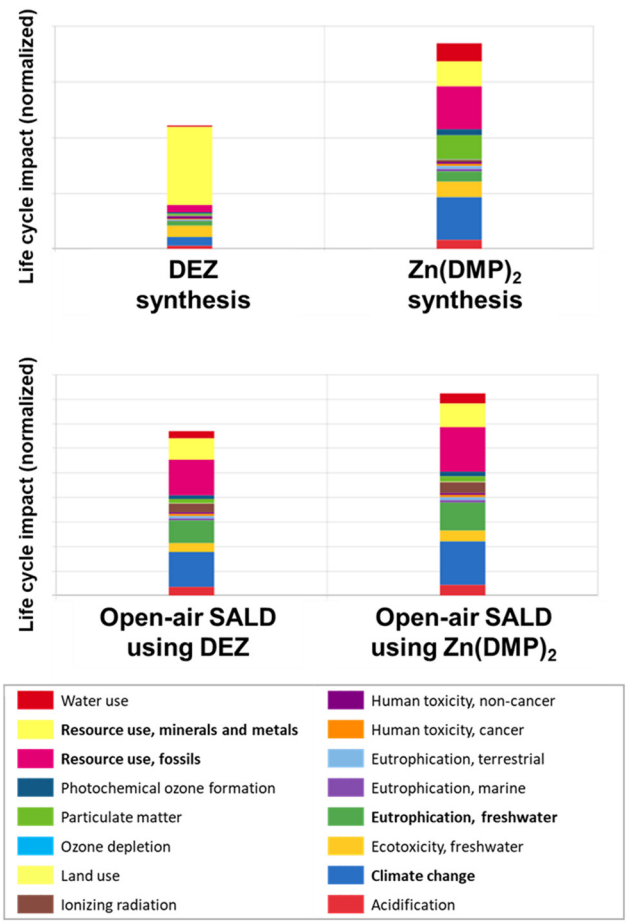

Fig. 8 Comparative LCA of DEZ *vs.* $Zn(DMP)_2$ in terms of Zn precursor synthesis and ZnO open-air SALD. The most strongly affected categories are written in bold in the legend.

For $Zn(DMP)_2$, however, the resource use contribution is far lower as the synthesis only requires using $ZnCl_2$ which can be derived using metallic zinc, which itself can be recycled from iron and steel processing.[43] For most other categories, however, we find the current $Zn(DMP)_2$ synthesis approach produces a worse environmental impact than DEZ. Part of this may be attributed to use of tetrahydrofuran (THF), a solvent which is typically produced from hydrocarbons out of the petrochemical industry, as is generally the case for ethers.[44] Separately, we may also expect the longer and more complex synthesis of $Zn(DMP)_2$ to have a considerable impact on the overall energy consumption of the synthesis, which has its own environmental footprint. To alleviate the impact of the solvent on $Zn(DMP)_2$ synthesis, other routes would need to be explored such as using THF produced from renewable sources[45] or another solvent such as 2-methyltetrahydrofuran which can be derived from biomass and has been suggested as an alternative to THF and Et_2O for Grignard reactions.[46,47]

Alternatively mechanochemistry may be used, which has already made great advancements in producing Grignard reagents for organic synthesis, minimizing the amount of ether solvents required to additive levels.[48,49] If a feasible transfer to metal chlorides as electrophiles could be realized, great improvements for product synthesis are achievable. Alternatively, mechanochemically performed alkali salt metathesis reactions have been proven to work opening another possible pathway for $Zn(DMP)_2$ synthesis.[50]

In contrast, the LCA for the open-air SALD process showed a very similar footprint for both precursors, with a relative improvement in the DEZ process across the board compared with the $Zn(DMP)_2$. This difference is mostly due to the faster growth rate which leads to a faster deposition and thus a lesser energy consumption linked with the various heating and electrical components as well as the nitrogen carrier gas consumption. As such, aiming for higher growth rates should be the main method to improve the deposition process environmental impact.

Conclusions

Through the use of open-air SALD, $Zn(DMP)_2$ could indeed be used to produce highly pure, crystalline ZnO thin films and at a higher speed than conventional ALD even when the latter uses DEZ. For temperatures where ALD conditions could be guaranteed (140 to 180 °C), these films grew along the *a*-axis, though textured *c*-axis oriented thin films could still be grown at 260 °C.

The environmental impact of the SALD process was shown to be larger for $Zn(DMP)_2$ insofar as the deposition lasted longer, resulting in a larger electricity consumption, while the greater impact of $Zn(DMP)_2$ synthesis step *versus* DEZ may be reduced by replacing THF with "greener" alternative solvents.

The conformality and functionality of the ZnO coatings could be verified in the context of protective coatings as Ag diffusion rate-controlling barriers to enhance the stability of ZnO/AgNW nanocomposite networks. These polycrystalline coatings were shown to be similar to their DEZ counterparts, though the anisotropic growth of ZnO produced using $Zn(DMP)_2$ combined with the high curvature present at the AgNW surface is suspected to have caused a higher ZnO coating roughness resulting in an easier Ag diffusion through less well protected regions, which could also have been caused by the slightly lower ZnO density observed.

Overall, $Zn(DMP)_2$ has shown to be a convenient alternative to DEZ, not despite—but thanks to its lower reactivity and volatility at room temperature, allowing it to be non-pyrophoric and therefore safer in transport and in open-air setups while maintaining thin film quality and functionality, while the high growth rate of DEZ was matched and even exceeded by $Zn(DMP)_2$ by opting for a high-throughput ALD approach such as SALD. These properties of $Zn(DMP)_2$ make it very versatile and easy to use especially in research environments, where flexibility is needed and changing experimental setups are common.

Data availability

The data used in this article (including Origin spreadsheets, images, and videos) are publicly available in the ESI† and at the Figshare repository at the following link: **https://doi.org/10.6084/m9.figshare.26202329.v1**.

Author contributions

L. Johnston: SALD deposition optimization, data collection and analysis for ellipsometry, GIXRD and XRR, SEM, and electrical characterization. Paper conception, writing, and figures. J. Obenlüneschloß: $Zn(DMP)_2$ synthesis, editing and paper conception. M. F. Khan Niazi: LCA study and interpretation. M. Weber: supervision, LCA study, XPS data collection, paper conception, editing and review. C. Lausecker: SALD deposition optimization, GIXRD and XRR. L. Rapenne: TEM and SAED data collection. H. Roussel: GIXRD and XRR analysis. C. Velasquez Sanchez: AgNW networks deposition and electrical characterization. D. Bellet: review, editing, and characterization analysis for AgNW. A. Devi: supervision, paper conception, review, and editing. D. Muñoz-Rojas: supervision paper conception, administration, project management, review, and editing.

Conflicts of interest

There are no conflicts to declare.

Acknowledgements

This research work was funded by the joint ANR-DFG project REACTIVE and the authors gratefully acknowledge ANR and DFG for the funding (ANR project number 21-CE08-0047 and DFG project number 490773082). LJ acknowledges the Ministère de l'Enseignement supérieur et de la Recherche in France for a Ph.D. grant. This work was performed within the framework of the Centre of Excellence of Multifunctional Architectured Materials "CEMAM" number ANR-10-LABX-44-01. Damien Evrard is thanked for support on the LCA part.

Notes and references

1 J. R. Van Ommen, A. Goulas and R. Puurunen, in *Kirk-Othmer Encyclopedia of Chemical Technology*, 2021.
2 M. Ritala, K. Kukli, A. Rahtu, P. I. Räisänen, M. Leskelä, T. Sajavaara and J. Keinonen, *Science*, 2000, **288**, 319–321.
3 C. Lausecker, D. Muñoz-Rojas and M. Weber, *Crit. Rev. Solid State Mater. Sci.*, 2023, 1–23.
4 M. Weber, E. Coy, I. Iatsunskyi, L. Yate, P. Miele and M. Bechelany, *CrystEngComm*, 2017, **19**, 6089–6094.
5 N. P. Dasgupta, X. Meng, J. W. Elam and A. B. F. Martinson, *Acc. Chem. Res.*, 2015, **48**, 341–348.
6 M. Moret, A. Abou Chaaya, M. Bechelany, P. Miele, Y. Robin and O. Briot, *Superlattices Microstruct.*, 2014, **75**, 477–484.
7 T. Abu Ali, J. Pilz, P. Schäffner, M. Kratzer, C. Teichert, B. Stadlober and A. M. Coclite, *Phys. Status Solidi A*, 2020, **217**, 2000319.
8 E. Guziewicz, M. Godlewski, T. Krajewski, Ł. Wachnicki, A. Szczepanik, K. Kopalko, A. Wójcik-Głodowska, E. Przeździecka, W. Paszkowicz, E. Łusakowska, P. Kruszewski, N. Huby, G. Tallarida and S. Ferrari, *J. Appl. Phys.*, 2009, **105**, 122413.
9 T. Tynell and M. Karppinen, *Semicond. Sci. Technol.*, 2014, **29**, 043001.
10 L. Mai, F. Mitschker, C. Bock, A. Niesen, E. Ciftyurek, D. Rogalla, J. Mickler, M. Erig, Z. Li, P. Awakowicz, K. Schierbaum and A. Devi, *Small*, 2020, **16**, 1907506.
11 E. B. Yousfi, J. Fouache and D. Lincot, *Appl. Surf. Sci.*, 2000, **153**, 223–234.
12 B. S. B. Sang and M. K. M. Konagai, *Jpn. J. Appl. Phys.*, 1996, **35**, L602.
13 S.-H. K. Park, C.-S. Hwang, H.-S. Kwack, J.-H. Lee and H. Y. Chu, *Electrochem. Solid-State Lett.*, 2006, **9**, G299.
14 A. Philip, L. Mai, R. Ghiyasi, A. Devi and M. Karppinen, *Dalton Trans.*, 2022, **51**, 14508–14516.
15 S. H. Han, R. E. Agbenyeke, G. Y. Lee, B. K. Park, C. G. Kim, Y. K. Lee, S. U. Son and T.-M. Chung, *Dalton Trans.*, 2020, **49**, 4306–4314.
16 R. O. Donoghue, D. Peeters, D. Rogalla, H.-W. Becker, J. Rechmann, S. Henke, M. Winter and A. Devi, *Dalton Trans.*, 2016, **45**, 19012–19023.
17 S. Stefanovic, N. Gheshlaghi, D. Zanders, I. Kundrata, B. Zhao, M. K. S. Barr, M. Halik, A. Devi and J. Bachmann, *Small*, 2023, **19**, 2301774.
18 D. Muñoz-Rojas, V. H. Nguyen, C. Masse de la Huerta, S. Aghazadehchors, C. Jiménez and D. Bellet, *C. R. Phys.*, 2017, **18**, 391–400.
19 D. Muñoz-Rojas and J. MacManus-Driscoll, *Mater. Horiz.*, 2014, **1**, 314–320.

20 C. A. M. de la Huerta, V. H. Nguyen, A. Sekkat, C. Crivello, F. Toldra-Reig, P. B. Veiga, S. Quessada, C. Jimenez and D. Muñoz-Rojas, *Adv. Mater. Technol.*, 2020, **5**, 2000657.
21 H. K. Hofstee, J. Boersma, J. D. van der Meulen and G. J. M. van der Kerk, *J. Organomet. Chem.*, 1978, **153**, 245–252.
22 L. Mai, D. Zanders, E. Subaşı, E. Ciftyurek, C. Hoppe, D. Rogalla, W. Gilbert, T. de los Arcos, K. Schierbaum, G. Grundmeier, C. Bock and A. Devi, *ACS Appl. Mater. Interfaces*, 2019, **11**, 3169–3180.
23 V. H. Nguyen, J. Resende, C. Jiménez, J.-L. Deschanvres, P. Carroy, D. Muñoz, D. Bellet and D. Muñoz-Rojas, *J. Renewable Sustainable Energy*, 2017, **9**, 021203.
24 L. Bardet, D. T. Papanastasiou, C. Crivello, M. Akbari, J. Resende, A. Sekkat, C. Sanchez-Velasquez, L. Rapenne, C. Jiménez, D. Muñoz-Rojas, A. Denneulin and D. Bellet, *Nanomaterials*, 2021, **11**, 2785.
25 A. Khan, V. H. Nguyen, D. Muñoz-Rojas, S. Aghazadehchors, C. Jiménez, N. D. Nguyen and D. Bellet, *ACS Appl. Mater. Interfaces*, 2018, **10**, 19208–19217.
26 T. Sannicolo, N. Charvin, L. Flandin, S. Kraus, D. T. Papanastasiou, C. Celle, J.-P. Simonato, D. Muñoz-Rojas, C. Jiménez and D. Bellet, *ACS Nano*, 2018, **12**, 4648–4659.
27 T. Muneshwar and K. Cadien, *J. Appl. Phys.*, 2018, **124**, 095302.
28 C. R. Ellinger and S. F. Nelson, *Chem. Mater.*, 2014, **26**, 1514–1522.
29 V. Consonni and A. M. Lord, *Nano Energy*, 2021, **83**, 105789.
30 V. Lujala, J. Skarp, M. Tammenmaa and T. Suntola, *Appl. Surf. Sci.*, 1994, **82–83**, 34–40.
31 S.-Y. Pung, K.-L. Choy, X. Hou and C. Shan, *Nanotechnology*, 2008, **19**, 435609.
32 B. Xia, J. J. Ganem, E. Briand, S. Steydli, H. Tancrez and I. Vickridge, *Vacuum*, 2021, **190**, 110289.
33 V. H. Nguyen, A. Sekkat, C. Jiménez, D. Muñoz, D. Bellet and D. Muñoz-Rojas, *Chem. Eng.*, 2021, **403**, 126234.
34 V. H. Nguyen, U. Gottlieb, A. Valla, D. Muñoz, D. Bellet and D. Muñoz-Rojas, *Mater. Horiz.*, 2018, **5**, 715–726.
35 G. Brunin, F. Ricci, V.-A. Ha, G.-M. Rignanese and G. Hautier, *npj Comput. Mater.*, 2019, **5**, 1–13.
36 D. T. Papanastasiou, A. Schultheiss, D. Muñoz-Rojas, C. Celle, A. Carella, J.-P. Simonato and D. Bellet, *Adv. Funct. Mater.*, 2020, **30**, 1910225.
37 L. Bardet, M. Akbari, C. Crivello, L. Rapenne, M. Weber, V. H. Nguyen, C. Jiménez, D. Muñoz-Rojas, A. Denneulin and D. Bellet, *ACS Appl. Nano Mater.*, 2023, **6**, 15234–15246.
38 M. F. K. Niazi, D. Muñoz-Rojas, D. Evrard and M. Weber, *ACS Sustainable Chem. Eng.*, 2023, **11**, 15072–15082.
39 M. Weber, N. Boysen, O. Graniel, A. Sekkat, C. Dussarrat, P. Wiff, A. Devi and D. Muñoz-Rojas, *ACS Mater. Au*, 2023, **3**, 274–298.
40 C. R. Noller, *Org. Synth.*, 1932, **12**, 86.
41 D. Seyferth, *Organometallics*, 2001, **20**, 2940–2955.
42 U.S. Department of Energy, *Critical Materials Assessment*, 2023.
43 C. A. Basha, P. C. Warrier, A. L. Alagappan, K. V. Venkateswaran, R. Vijayavalli, P. V. Vasudeva Rao and H. V. K. Udupa, *J. Electroanal. Chem. Interfacial Electrochem.*, 1981, **118**, 365–374.
44 L. Karas and W. J. Piel, in *Kirk-Othmer Encyclopedia of Chemical Technology*, ed. Kirk-Othmer, Wiley, 2000.
45 H. E. Hoydonckx, W. M. Van Rhijn, W. Van Rhijn, D. E. De Vos and P. A. Jacobs, in *Ullmann's Encyclopedia of Industrial Chemistry*, Wiley, 1st edn, 2007.
46 A. Kadam, M. Nguyen, M. Kopach, P. Richardson, F. Gallou, Z.-K. Wan and W. Zhang, *Green Chem.*, 2013, **15**, 1880–1888.
47 K. Alorku, C. Shen, Y. Li, Y. Xu, C. Wang and Q. Liu, *Green Chem.*, 2022, **24**, 4201–4236.
48 P. Gao, J. Jiang, S. Maeda, K. Kubota and H. Ito, *Angew. Chem., Int. Ed.*, 2022, **61**, e202207118.
49 R. Takahashi, A. Hu, P. Gao, Y. Gao, Y. Pang, T. Seo, J. Jiang, S. Maeda, H. Takaya, K. Kubota and H. Ito, *Nat. Commun.*, 2021, **12**, 6691.
50 R. F. Koby, N. R. Rightmire, N. D. Schley, T. P. Hanusa and W. W. Brennessel, *Beilstein J. Org. Chem.*, 2019, **15**, 1856–1863.